College of Engineering

On the determination of spherical nanoindentation stress–strain curves

Sandip Basu, Alexander Moseson, and Michel W. Barsoum[a)]
Department of Materials Science and Engineering, Drexel University, Philadelphia, Pennsylvania 19104

Instrumented nanoindentation experiments, especially with sharp tips, are a well-established technique to measure the hardness and moduli values of a wide range of materials. However, and despite the fact that they can accurately delineate the onset of the elasto-plastic transition of solids, spherical nanoindentation experiments are less common. In this article we propose a technique in which we combine (i) the results of continuous stiffness measurements with spherical indenters – with radii of 1 μm and/or 13.5 μm, (ii) Hertzian theory, and (iii) Berkovich nanoindentations, to convert load/depth of indentation curves to their corresponding indentation stress–strain curves. We applied the technique to fused silica, aluminum, iron and single crystals of sapphire and ZnO. In all cases, the resulting indentation stress–strain curves obtained clearly showed the details of the elastic-to-plastic transition (i.e., the onset of yield, and, as important, the steady state hardness values that were comparable with the Vickers microhardness values obtained on the same surfaces). Furthermore, when both the 1 μm and 13.5 μm indenters were used on the same material, for the most part, the indentation stress–strain curves traced one trajectory. The method is versatile and can be used over a large range of moduli and hardness values.

I. INTRODUCTION

In the past 20 years, instrumented nanoindentation experiments have emerged as a powerful tool in understanding the mechanical behavior of solids in general, and single crystals and thin films in particular. However, since the majority of the work has been carried out using Berkovich indenters, the emphasis has been more on extracting moduli and hardness values.[1] Berkovich or cube corner indenters are quite sharp and result in plastic deformation almost instantly; consequently, much of the information about the purely elastic region and, as important, the elastic-to-plastic transition is lost, a fact that has long been appreciated.[2]

As discussed herein, that information can be readily obtained by using spherical indenters. To do so, however, use is made of the continuous stiffness measurement technique (CSM), a technique with which it is possible to apply a load to the indenter tip, while simultaneously superimposing an oscillating force, with force amplitudes that are roughly an order of magnitude smaller than the nominal load.[3] This technique is thus capable of accurately measuring the contact stiffness at every load and eliminates the need to carry out multiple loading–

unloading measurements, as described in the Field and Swain method,[4,5] to calculate the variations in hardness and moduli values with load and displacement into the surface.

Given that the conversion of load–displacement curves to indentation stress–strain curves is almost as old as the technique of using indentations to probe the mechanical properties of solids,[2] it is somewhat surprising that this conversion is not much more common than it is. This comment notwithstanding, there have been a number of papers in which spherical nanoindenters have been used.[4,6–9] Roughly a decade ago, Field and Swain suggested a method to extract indentation stress–strain curves from load–displacement curves.[5,10] But for reasons that are not clear, and with some exceptions,[6–9,11,12] their methodology has not caught on and as importantly, Swain et al. have not used this technique in their more recent work. Instead, in some recent publications,[6,11,12] plots of hardness versus indentation penetration were presented, but none as indentation stress–strain curves. Before acquiring the CSM option, we used the Field and Swain method to convert load–displacement results obtained on Ti_3SiC_2,[13] and single crystals of mica[14] and graphite,[15] loaded parallel to the c-axis to indentation stress–strain curves.

Herbert et al.[7] described a methodology that is almost identical to the one described here and applied it to Al;

they concluded that the method was a qualified success in that more work was needed to better delineate the yield points of Al. Again for reasons that are not clear, and as far as we are aware, neither Pharr and coworkers, nor others, have attempted to develop the technique further.

In summary, and despite the use by some of spherical nanoindenters—and the ease by which the load can, in principle, be converted to stress—as far as we are aware, there has been little effort in trying to systematically study and convert nanoindentation load–displacement results to their corresponding stress–strain curves.

The objective of this article is to apply a variation of the Herbert et al.[7] technique to a number of quite different solids, namely amorphous silica, polycrystalline aluminum, Al, iron, Fe, and single crystals of sapphire and ZnO. In all cases, the results were compared with the moduli reported in the literature and those measured using the Oliver and Pharr[1] method and a Berkovich indenter. The hardness values obtained here were, in turn, compared with the results obtained using Vickers and Berkovich indenters. We show herein that this approach is quite powerful and versatile.

II. SPHERICAL INDENTATION MODEL

Typically, a nanoindentation test results in the load (P) and displacement into surface (h_t) data. Additionally, the CSM attachment provides the harmonic contact stiffness (S) values over the entire range of loading. The vast majority of spherical nanoindentation data analysis is based on the Hertz equation in the elastic region[1,2,5,10]

$$P = \frac{3}{4} E_{eff} R^{1/2} h_e^{3/2} \quad , \quad (1)$$

where R is the radius of the indenter, h_e is the elastic distance into the surface (Fig. 1), and E_{eff} is the system composite modulus given by

$$\frac{1}{E_{eff}} = \frac{1 - \nu^2}{E} + \frac{1 - \nu'^2}{E'} \quad , \quad (2)$$

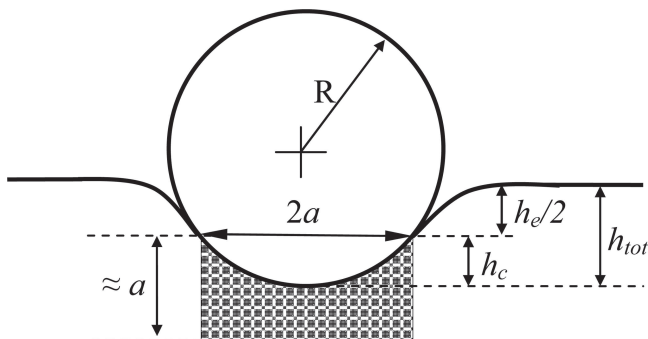where E' and ν', respectively, refer to the modulus and

FIG. 1. Schematic representation of spherical indentation.

Poisson's ratio of the diamond indenter (1140 GPa and 0.07). The other terms refer to those of the sample.

For a rigid spherical indenter, Sneddon[16] showed that the elastic displacements of a plane surface above and below the contact circle are equal, and given by

$$h_e = h_t = \frac{a^2}{R} \quad , \quad (3)$$

where a is the contact radius during indentation (Fig. 1). Combining Eqs. (1) and (3) yields

$$\frac{P}{\pi a^2} = \frac{4}{3\pi} E_{eff} \left(\frac{a}{R} \right) \quad . \quad (4)$$

The left side of the equation represents the indentation stress or mean contact pressure, also referred to as the Meyer hardness.[2] The expression in parentheses on the right side represents the indentation strain.[2] Henceforth in this article, these will be referred to as indentation stress and indentation strain, respectively. Note these are not the same as the stresses and strains measured in uniaxial compression tests.

In the remainder of this section we outline a method by which a can be calculated from a knowledge of P, S, and the total displacement of the indenter into the surface, h_t, first in the elastic regime, and then in the elasto-plastic regime.

A. Elastic regime

Both the Oliver and Pharr[1] and Field and Swain[5] methods use the slopes of the initial portions of the unloading curves, dP/dh, to calculate h_e. Differentiating Eq. (1) with respect to h yields

$$\frac{dP}{dh} = 2E_{eff} R^{1/2} h_e^{1/2} \quad , \quad (5)$$

which when substituted in Eq. (1), results in

$$P = \frac{2}{3} \frac{dP}{dh} h_e \quad . \quad (6)$$

Therefore,

$$h_e = \frac{3}{2} P \frac{dh}{dP} \quad . \quad (7)$$

Since dP/dh is nothing but the stiffness, S*, of the system composed of the specimen and the load frame, the stiffness of the material itself can be calculated from

$$\frac{1}{S} = \frac{1}{S^*} - \frac{1}{S_f} \quad , \quad (8)$$

where S_f is the load-frame stiffness, which in our case is

5.5 MN/m. This value is the one obtained from the manufacturer of the instrument. Replacing dP/dh in Eq. (8) with S, one obtains

$$h_e = \frac{3}{2}\frac{P}{S} \quad . \tag{9}$$

Once h_e is known, a is calculated from Eq. (3).

B. Elasto-plastic regime

Again following Oliver and Pharr[1] and Field and Swain[5] we assume the "contact depth", h_c, defined as the distance from the circle of contact to the maximum penetration depth (Fig. 1) to be given by

$$h_c \approx h_t - \frac{h_e}{2} \quad . \tag{10}$$

Combining Eqs. (9) and (10) yields

$$h_c = h_t - \frac{3}{4}\frac{P}{S} \quad . \tag{11}$$

For reasons discussed below, we modified this equation to read

$$h_c = h_t - \frac{3}{4}\frac{P}{S} + \delta \quad , \tag{12}$$

where δ is an adjustable parameters of the order of a few nm needed to obtain the correct elastic moduli.

Once h_c is known, a can be calculated assuming

$$a = \sqrt{2Rh_c - h_c^2} \approx \sqrt{2Rh_c} \quad . \tag{13}$$

Note the right-hand expression is only valid if $h_c \ll a$, and the indenter tip is perfectly spherical. In the purely elastic regime, $h_c = h_t/2 = h_e/2$ and Eq. (3) and Eq. (10) become identical. Also note that for the most part in the plastic regime, since $h_t \gg h_e/2$ and it follows that $h_c \approx h_t$ [Eq. (10)].

For an isotropic elastic solid, indented with a spherical indenter,[1]

$$a = \frac{S}{2E_{eff}} \quad . \tag{14}$$

To date the most commonly used method for measuring nanoindentation hardness values is the Oliver and Pharr method, in which h_c is calculated from Eq. (11), and the contact area, A, is determined from a calibrated area function of the form[1]

$$A(h_c) = C_0 h_c^2 + C_1 h_c + C_2 h_c^{1/2} + C_3 h_c^{1/4} + C_4 h_c^{1/8} + \ldots \quad . \tag{15}$$

In this paper we calculate a from Eq. (13). The validity of the results are then judged by two simple criteria. The first criterion is that the initial portion of the indentation stress–strain curves be linear, with the higher of two slopes: either the slope obtained from Eq. (14), or the one measured by the standard method, namely a Berkovich indenter and the Oliver and Pharr method. Second, that the stress level at higher strains corresponds to the stress measured on the same material using a Vickers microhardness indenter.

III. EXPERIMENTAL DETAILS

The nanoindenter (XP System, MTS, Oak Ridge, TN) used in this work was equipped with a CSM attachment. All tests were carried out with a load rate over load factor of 0.1. The harmonic displacement for the CSM was 2 nm with a frequency of 45 Hz. The tests were carried out to various loads for different materials depending on their hardness. Once the surface is detected, the indenter is loaded at a constant value of $(dP/dt)/P = 0.1$ (the loading rate divided by the load), which has the advantage of logarithmically scaling the data density so that there is just as much data at low loads as high. Constant $(dP/dt)/P$ tests also have the advantage of producing a constant indentation strain rate, $(dh/dt)/h$, provided the hardness is not a function of the depth.[17]

Two diamond spherical tips—with radii of 13.5 μm and 1 μm—were used. As noted in Sec. I, we used a number of materials: fused silica (GM Associates Inc., Oakland, CA); sapphire single crystal (C-orientation) (Kyocera Industrial Ceramics, Vancouver, WA); C-orientation ZnO single crystal (Wafer World, Inc., West Palm Beach, FL); and two metals: Al (Puratronic 99.999%, Alfa Aesar, MA) and Fe (99.99 % Alfa Aesar, MA).

In all cases, the Vickers microhardness values of the same surfaces used for the nanoindentations were measured using a microhardness indenter (M-400 Hardness Tester, LECO Corp., St. Joseph, MI) and a 10 N load. We also used the Oliver and Pharr[1] method and a Berkovich indenter tip to measure the hardness, H_{Br}, and moduli, E_{Br}, of all samples. The latter will henceforth be referred to as the standard method.

Lastly, to compare the indentation stress–strain curves with those measured in uniaxial compression, a Fe cylinder (9.7 mm diameter × 35 mm long) was loaded at a nominal stress rate of approximately 13.5 MPa/s. The strain was measured using an extensometer attached to the sample.

IV. RESULTS

A. Stiffness versus contact radii

Before plotting the indentation stress–strain curves it is crucial to determine the effective elastic stiffness of the various materials examined. According to Eq. (14), a plot of S versus a should result in straight lines with slopes proportional to E_{eff} as observed [Fig. 2(a)]. [The results for Al are not shown in Fig. 2(a), since they are almost identical to those for fused silica.] The linearity over the
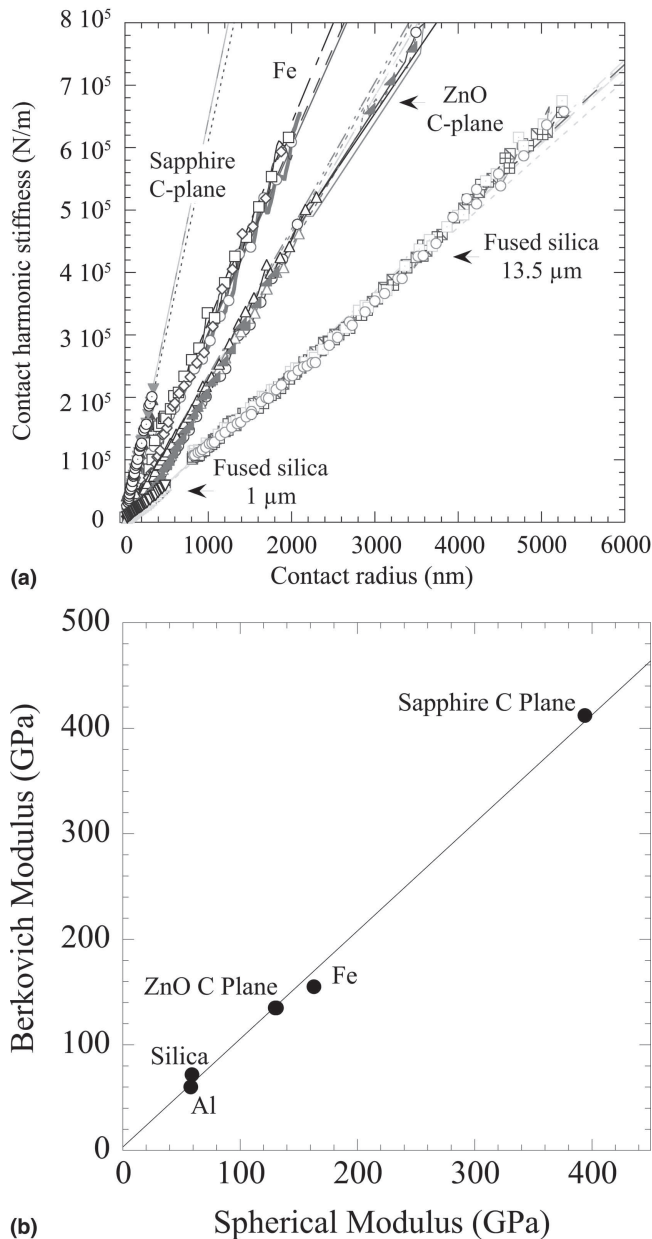
FIG. 2. (a) Plot of contact harmonic stiffness versus contact radius as determined from spherical nanoindentation; and (b) comparison of moduli values determined from Berkovich and spherical nanoindentation.

entire loading regime implies that S is not affected by pop-ins or plastic deformation. The reproducibility is also noteworthy—each group of results was obtained from multiple locations—as is the excellent agreement between the slopes obtained using the 1 μm and 13.5 μm indenters on fused silica and ZnO. (The 1-μm results are not shown.) In other words, E_{eff} is not a function of indenter radius, as one would expect. The moduli values calculated from both spherical and Berkovich nanoindentation were also compared in Fig. 2(b). The linear agreement between the values, for the wide range of

solids used during this work, shows the potential for using the spherical nanoindentation technique in parallel to the more famous Berkovich technique.

The Young's moduli values calculated from Eqs. (2) and (14) are listed in Table I as E_{Sp} (column 4) together with the literature data, E, (column 3) and the values determined using the standard method, namely E_{Br} (column 5). Comparison of the former two sets of results make it amply clear that $E_{Sp} < E$. Similarly, and with the exception of Fe, $E_{Sp} < E_{Br}$. The good correlation between E_{Sp} and E_{Br} [Fig. 2(b)] suggests that the determination of moduli with spherical indentors is as valid as the more common standard method.

B. Moduli corrections

Given that the standard method is a well-established technique to measure moduli, we used it to determine E_{Br} as we assumed the latter to be the correct modulus but only if $E_{Sp} < E_{Br}$. If $E_{Sp} > E_{Br}$ we assumed the former to be more correct. The reason is simple: experimentally, there are many reasons one can obtain lower moduli, but it is difficult to conceive of a scenario where the measured moduli would be higher than actual. In other words, the higher the modulus the closer it must be to the true modulus. This conclusion is corroborated in this work; in all cases, the moduli measured, whether E_{Br} or E_{Sp} were < E.

After plotting the indentation stress–strain curves from the as-received data, δ was adjusted so that the linear, or elastic portions of the indentation stress–strain curves corresponded to E_{Br}. In most cases that entailed positive δ-values. Once the latter were plotted they were shifted mechanically so all plots passed through the origin. In the case of Fe, where $E_{Sp} > E_{Br}$, we assumed E_{Sp} to be the more correct value, and the curves were simply mechanically shifted.

To best illustrate this methodology, consider the indentation stress–strain results for Al shown in Fig. 3(a). [A typical load/depth of penetration curve is shown in the inset in Fig. 3(a).] While the steady state stresses converge onto the dashed horizontal line representing the Vickers hardness of the same surface (Table I), the initial portions varied from location to location. The inset in Fig. 3(b) illustrates the effect of increasing δ on the shapes of the indentation stress–strain curves shown in Fig. 3(a). With one exception, where δ = 25 nm, the shifts required for the elastic portions of the curves to correspond to E_{Br} were of the order of 10 nm. The mechanically shifted curves are shown in Fig. 3(b). In addition to obtaining the higher moduli, shifting the curves by δ, has the added advantage of rotating the initial points in Fig. 3(a) counterclockwise in such a way that they now all fall on the same straight line as the other data points [Fig. 3(b)]. The initial hump is also greatly reduced.

TABLE I. Summary of Poisson's ratios, v, and Young's moduli, E, or $1/s_{33}$ taken from the literature, the moduli values measured in this work using the spherical indenters, E_{Sp}, a Berkovich indenter, E_{Br}, and the hardness values using the latter, H_{Br}. Also listed in last column are the Vickers microhardness values measured herein using a load of 10 N.

Material	v	E or $1/s_{33}$ (GPa)	E_{Sp} (Fig. 2) (GPa)	E_{Br} (GPa)	H_{Br} (GPa)	Vickers μ-Hardness (GPa)
Silica 13.5 μm	0.18	72	59 ± 1	71.7 ± 0.7	9.3 ± 0.2	5.6 ± 0.6[b]
SiO$_2$ 1 μm			59 ± 2			
Al 13.5 μm	0.3	70	58 ± 4	60 ± 4	0.48 ± 0.02	0.29 ± 0.02
Fe 13.5 μm	0.3	210	163 ± 9	155 ± 1	1.2 ± 0.1	1.3 ± 0.1
		203[a]				
C-ZnO 13.5 μm	0.2	$1/s_{33}$ = 149	130 ± 4	135 ± 3	4.8 ± 0.2	3.3 ± 0.1
C-ZnO 1 μm			131 ± 4			
C-Al$_2$O$_3$ 1 μm	0.2	$1/s_{33}$ = 458	394 ± 4	412 ± 8	25 ± 1	22.5[c]

[a] This work.

[b] This value depends on load; lower loads yield higher values.

[c] According to manufacturer.

In the remainder of this article we discuss each material separately starting with the standard material of choice, fused silica.

C. Fused silica

Typical load-displacement curves for the 1 μm and 13.5 μm indenters on fused silica are shown in Fig. 4(a). Figure 4(b) plots the indentation stress–strain curves [i.e., Eq. (4)], for five different locations, for both the 1 μm and 13.5 μm indenters; the results for the latter were shifted by 0.3, to the right for clarity's sake. The reproducibility of the 13.5-μm results is excellent, those of the 1 μm ones less so, but acceptable, nevertheless. Least squares fits of the linear portions in Figs. 2(a) and 4(b) yield slopes that correspond to an E_{Sp} 59 ± 2 GPa (Table I), rather than the established value of 72 GPa measured by the standard method. Figure 4(c) re-plots the results shown in Fig. 4(b), after the δ-correction and the mechanical shift of the curves. The range of δ-correction was quite small: ± 1.5 nm. The curves derived from the 1 μm and 13.5 μm indentations [Fig. 4(c), open squares] appear to superimpose onto each other lending great validity to our method. In other words, in the case of fused silica, the results obtained, after the yield point, do not depend on the indenter diameter. [For the sake of clarity only one indentation stress–strain curve from the 13.5-μm data set is plotted in Fig. 4(c). The spread in the results for five locations was no more than the widths of five symbols across.]

Based on Fig. 4(c), a clear "yield" point is observed for both indenters at ≈ 6.5 ± 1 GPa. Interestingly, this yield point occurs at a stress that is slightly higher than the 5.6 ± 0.6 GPa obtained from our Vickers microhardness measurements for the same sample at 10 N. (Higher microhardness values are obtained at lower loads.) Whether this is simply coincidental remains to be determined. The

nature of the micro-yielding is not clear at this time, but is most probably related to the densification of the amorphous silica under the indenter.

Note that our method is valid for the 1 μm indenter tip only up to h_t depths of the order of ≈300 nm. Above that the tip is no longer spherical and Eq. (12) is not valid, which is why there are no results beyond a strain of 0.7 in Fig. 4(c). This is not a problem for the 13.5 μm indenter until penetration depths of ~4500 nm, but the maximum load applicable was 700 mN [Fig. 4(a)]. To obtain the entire range of stresses for silica with one indenter, its diameter would have to fall in between the ones used here.

D. ZnO

The typical load-displacement curves obtained when the ZnO C-planes are indented with the 13.5 μm indenter [Fig. 5(a)] are characterized by large pop-ins that occur between 80 mN and 120 mN depending on location. When these results are converted into indentation stress–strain plots [Fig. 5(b)] it is obvious that the response is linear elastic up to a maximum stress of 6.5 ± 1 GPa, before dropping substantially to just under 3 GPa, before slowly rising with further strain. The average δ's needed to obtain the E_{Br} of 135 GPa, were 4.5 ± 2 nm and all positive.

By design the initial slopes of the indentation stress–strain curves obtained using the 1 μm tip [Fig. 5(b), crosses] were identical to those obtained using the larger diameter indenter. The average δ was 3.7 ± 2.5 nm and positive. For the sake of clarity only one indentation stress–strain curve of the 1 μm indenter was plotted in its entirety (crosses). For the other locations only the region for which the strain >0.25 were plotted. At ≈6 ± 1 GPa, the peak stresses (not shown) were statistically indistinguishable to those measured using the 13.5 μm indenter.
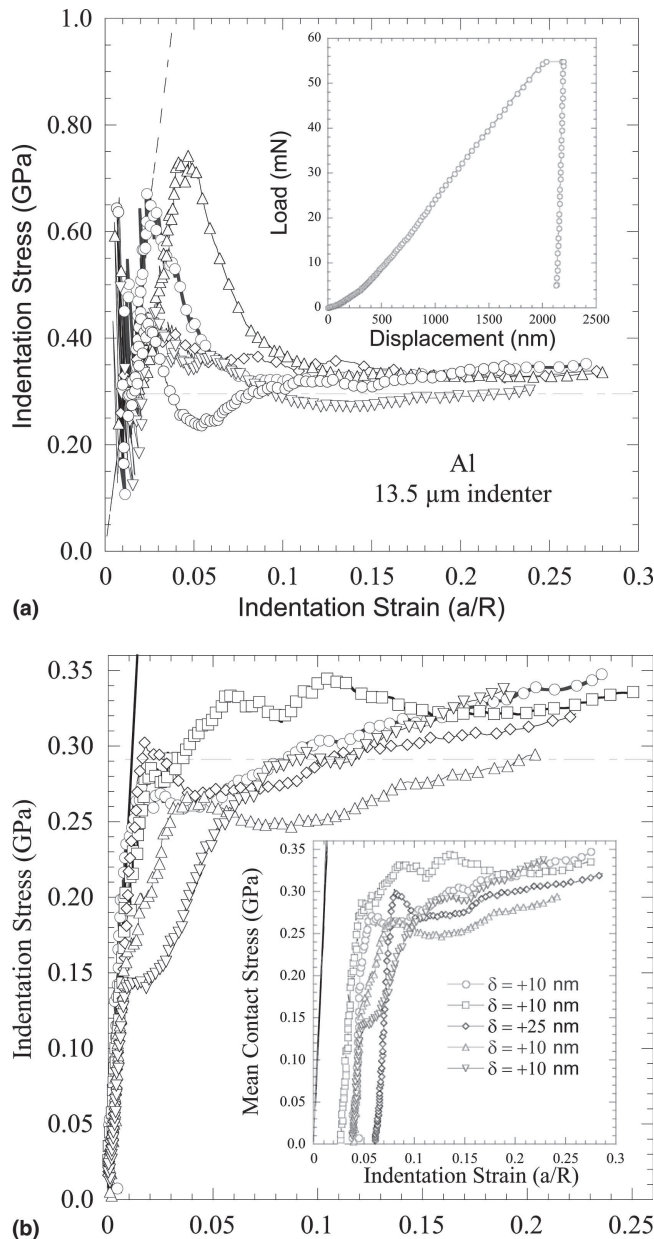
FIG. 3. Indentation stress/strain curves in pure Al in various locations, (a) as-received data. Inset shows a typical load/depth-of-penetration curve, (b) same as (a), but after δ−correction (see text) and mechanical shifting of curves. Inset shows the results before mechanical shifting. The numbers listed in the inset represent the values of δ needed to obtain the correct modulus. Note shifting the curve also rotates the initial nonsensical points counterclockwise and aligns them with the other results. Dashed horizontal lines represent the Vickers microhardness values measured on the same Al sample.

After the pop-ins, the hardness values (not shown) drop to ≈3.5 ± 1 GPa, before increasing more or less linearly with strain. For reasons that are not clear, but could be related to the indenter size effect, the hardness values calculated from the 1 μm indentions appear to be ≈1 GPa higher than those measured using the 13.5 μm indenta-

tions. The Vickers microhardness values on the same surface were ≈3.3 ± 0.1 GPa (Table I).

E. Sapphire

Typical load-displacement curves obtained when the *C*-planes of sapphire are loaded with the 1 μm indenter are characterized by a "pop-in" event at a load of ≈15 mN.[18] The corresponding indentation stress–strain curves (Fig. 6) are characterized by a linear elastic region, with E_{Br} ≈412 ± 8 GPa (Table I). Because of the pop-ins, at ≈45 ± 4 GPa the stresses drop precipitously to ≈28 GPa, before rising more or less linearly with further penetration of the indenter. (In Fig. 6 the points to the left of the elastic line were erased.) Note that for sapphire the limit for the 1 μm indenter occurs at a strain of ≈0.5.

A more thorough and detailed study of spherical nanoindentations into *C*- and *A*- sapphire planes can be found in Ref. 18. In that work we show the deformation under the indenter was solely dislocation-based and dominated by basal slip, even at room temperature. We also showed that there is little plastic deformation before the pop-ins.

F. Iron

Here since $E_{Sp} > E_{Br}$, the indentation stress–strain curves for pure Fe were plotted assuming δ = 0 [Fig. 7(a)]. Inset in Fig. 7(a) shows a typical load-displacement curve. The mechanically shifted curves— for which the points to the left of the elastic line were removed—are shown in Fig. 7(b).

At 1.1 ± 0.1 GPa, the steady-state hardness values are in reasonably good agreement with the 1.3 ± 0.1 GPa Vickers microhardness value measured on the same sample [horizontal dashed line in Fig. 7(b)]. To compare the uniaxial compression results with those shown in Fig. 7(b) we multiplied the former stress by three and the strain by a factor of 10. The agreement between yield values of the two sets of results is surprisingly good.

G. Aluminum

The Al results were shown in Fig. 3 and discussed above. The initial variations in the indentation stress–strain response for the different locations [Fig. 3(a)] were ironed out by assuming δ-values in the order of 10 nm (with one exception in which δ = 25). The reproducibility of the shifted curves is noteworthy; especially when it is appreciated that the Al tested was polycrystalline.

The elastic-to-plastic transition for a majority of the curves is sharp and the stresses obtained hovered around the Vickers microhardness value measured on the same sample, namely 0.29 ± 0.02 GPa (Table I).
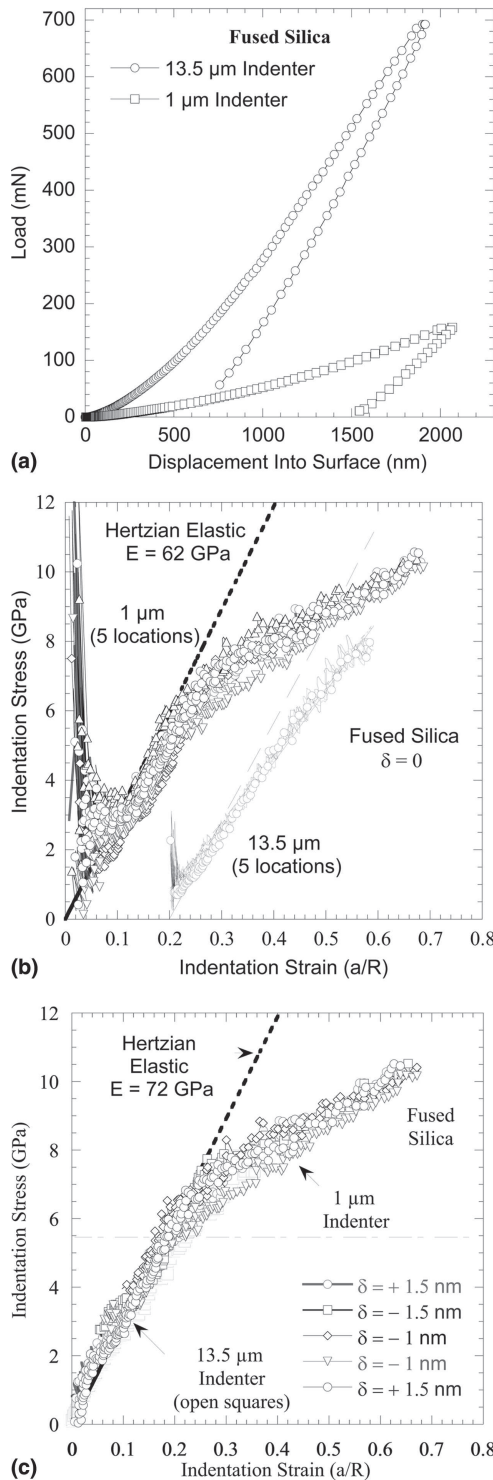
(a)

(b)

(c)

FIG. 4. Indentation results for fused silica, (a) load/depth-of-penetration results for the 1 μm and 13.5 μm indenters used, (b) corresponding stress–strain curves with no-correction (i.e., δ = 0); the 13.5 μm results are shifted by 0.2 to the right for clarity. (c) Same results after δ−correction, the values of which are listed. In this figure we eliminated the data points to the left of the dashed line, which represents the elastic response of the solid. Also shown is a typical result obtained using the 13.5 μm indenter. The agreement between the two sets of results in excellent. Dashed horizontal lines represent the Vickers microhardness values measured on the same silica.
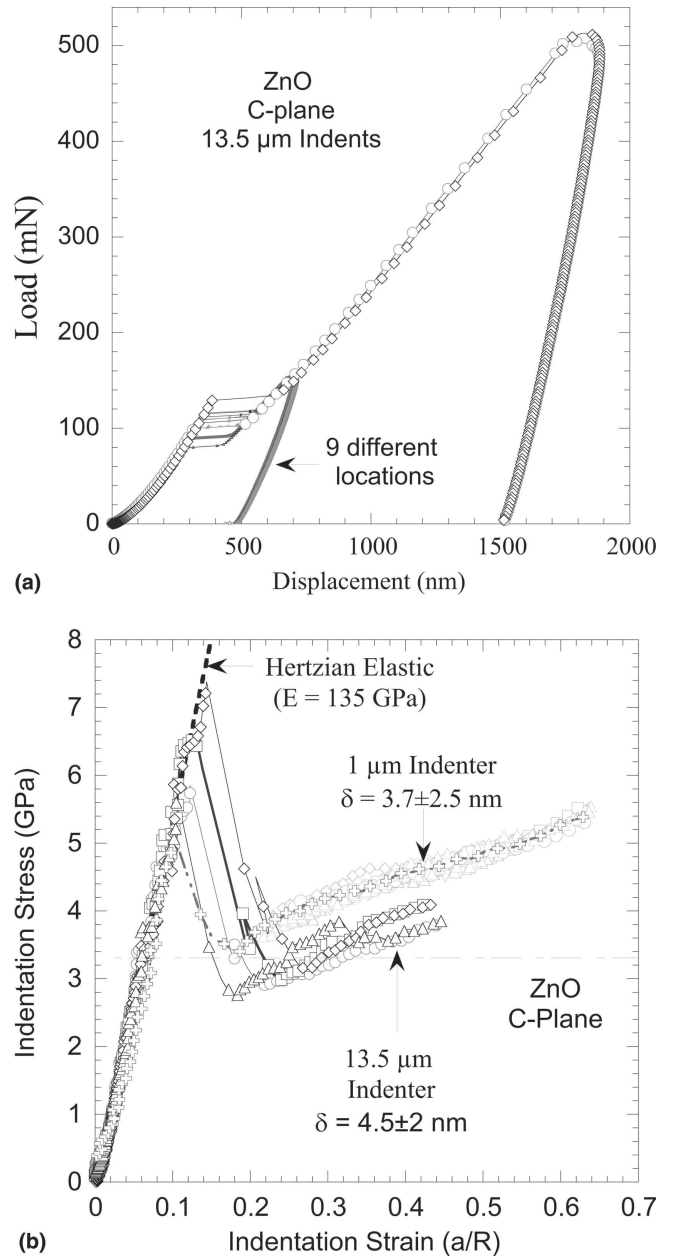

(a)

(b)

FIG. 5. Indentation results for single crystal ZnO C-planes, (a) load/depth-of-penetration results 13.5 μm indenter. Note large pop-ins around 100 mN. (b) Corresponding stress–strain curves after δ−correction and mechanical shifting. Here again data points to the left of the dashed line were removed. Dashed horizontal lines represent the Vickers microhardness values measured on the same ZnO C-planes.

V. DISCUSSION

A. Critical analysis of method

Based on the totality of the results, there is little doubt that our method is a relatively simple way to convert indentation load-penetration results into the much more informative and useful indentation stress–strain curves. The method is versatile and is applicable to Al, as well as sapphire, that between them span quite a large moduli
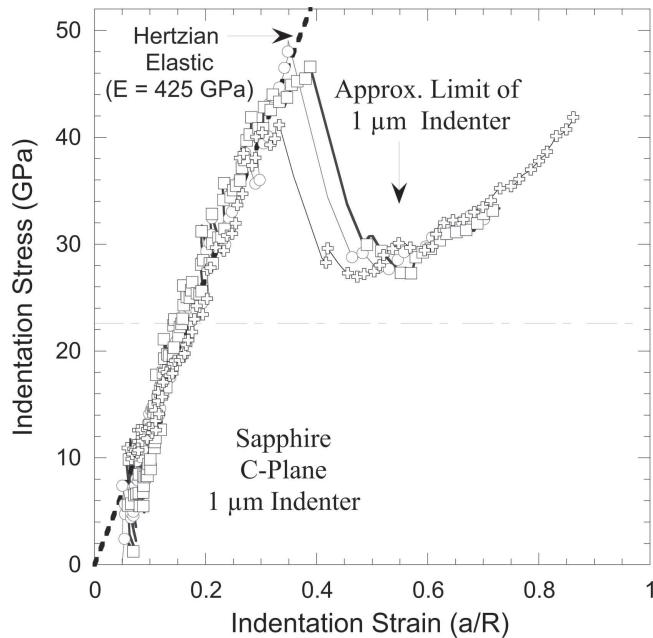
FIG. 6. Indentation stress–strain curves after δ–correction and mechanical shifting for single crystal sapphire *C*-planes loaded with a 1 μm radius spherical indenter. Note large pop-ins in the 40–50 GPa range. Dashed horizontal lines represent the Vickers microhardness values reported by the manufacturer for the same surface.

and hardness values range. The method is relatively straightforward and with the exception of a small δ-correction, otherwise devoid of adjustable parameters and/or any calibration procedures. The approach described herein was not arrived at easily; for over 2 years we tried and discarded numerous techniques before choosing the one described herein. Note that for the most part, the same conclusions are reached if δ = 0.

The usefulness and acceptance of the method proposed here depends on a number of factors, the most important of which is whether the resulting indentation stress–strain curves yield new information that is reliable, reproducible, and meaningful. To answer these questions we compare the results obtained in this work to previous work, with special emphasis on the hardness and moduli values obtained by the standard method.

B. Fused silica

It is clear from the results shown in Fig. 4(c) that the indentation stress–strain curves derived from the 1 μm and the 13.5 μm indenters are superimposable, not only at stresses below the ≈7 GPa "yield" point, but as important above that value. In other words, for silica we do not observe the indentation size effect that is well documented in the literature and observed below for ZnO.

C. ZnO

The modulus for ZnO calculated from Fig. 2(a), 130 ± 4 GPa, is close to the value of 111 ± 5 GPa, reported by
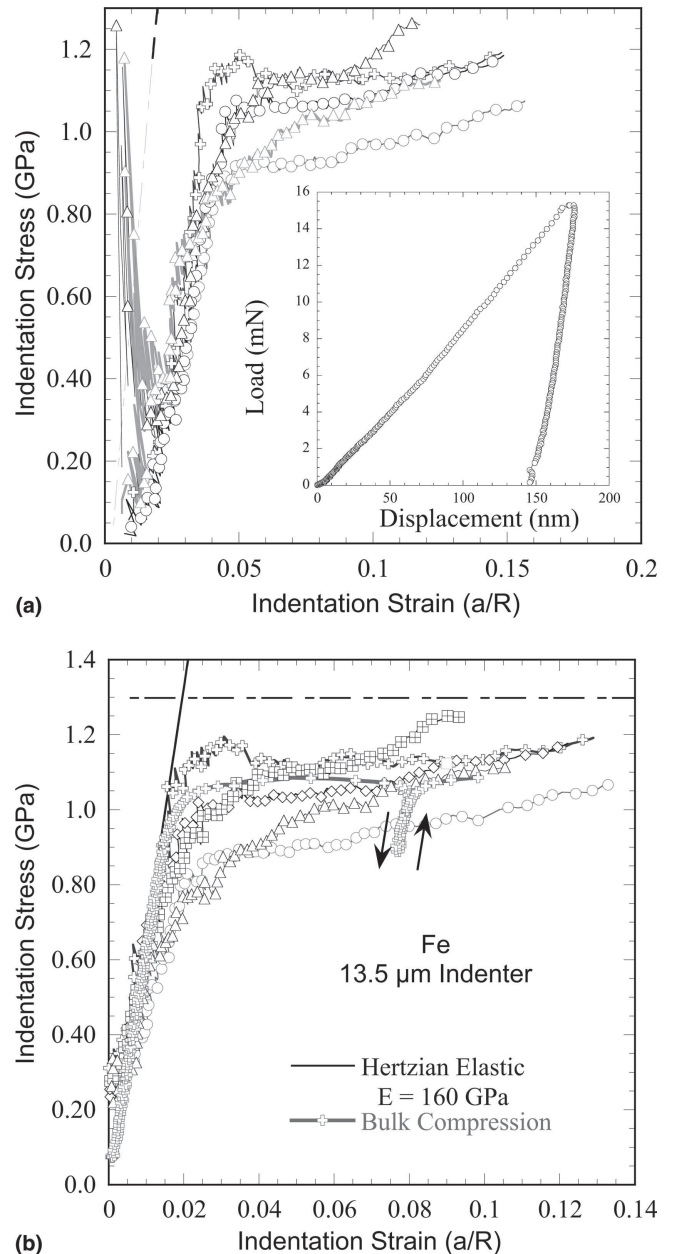

(a)

(b)

FIG. 7. Indentation stress–strain curves for Fe loaded with a 13.5 μm radius spherical indenter (a) before δ–correction. Inset shows typical indentation results. (b) Same results after mechanical shifting and δ–correction, the values of which are shown. Also plotted are bulk compression results (open squares) on the same Fe after multiplying the stress by 3 and the strain by 10. The agreement between the two sets of results is excellent. Dashed horizontal lines represent the Vickers microhardness values measured herein on the same sample.

Kucheyev et al.[12] on *C*-planes of ZnO, determined using the Field and Swain method[5] with a 4.2 μm radius indenter. Our value is also slightly lower than the value of $1/s_{33}$, namely 149 GPa, one would expect if a ZnO crystal were uniformly loaded along the *c*-axis. (The elastic constants were taken from Ref. 19.) The value of E_{Br} obtained—and ultimately used in Fig. 5(b), 135 GPa—is

in even better agreement with $1/s_{33}$. That the measured stiffness would be slightly lower than $1/s_{33}$ is expected given the highly nonuniform nature of the stress under an indenter. These results are crucial because they provide independent evidence that our technique and procedures of extracting the moduli values are valid on a near model system.

The hardness values immediately after the pop-ins seem to straddle the Vickers microhardness value of 3.5 GPa, measured herein on the same substrate [Fig. 5(b) and Table I]. Why the hardness continues to increase is unclear at this time, but could be related to work hardening. Interestingly, Kucheyev et al.[12] report a steady-state hardness value of 5.0 ± 0.1 GPa, and no work hardening whatsoever. More careful work is needed to better understand what is occurring beyond the pop-in stresses.

D. Sapphire

At 412 GPa, the moduli calculated from Berkovich nanoindentation for sapphire are ≈10% smaller than $1/s_{33}$, namely 458 GPa, one would expect had the crystal been uniformly loaded. (The elastic constants were taken from Ref. 20.) Here again these values are quite reasonable given the highly nonuniform nature of the load under the indenter. The modulus value measured from the "S" versus "a" plot is slightly lower compared with E_{Br} (Table I).

At ≈28 GPa, the minimum hardness values after the pop-ins in Fig. 6 are higher than those reported by the manufacturer, or those measured by the standard method (Table I). The increase in hardness values beyond the minimum is most probably an artifact of our methodology because Eq. (12) is not valid beyond a strain of ~0.5.

E. Iron

For reasons that are not clear, the values of E_{Br} and E_{Sp} we measure for Fe (Table I) are ≈30% lower than the value of 211 GPa reported in the literature, or the 203 GPa we obtained from our uniaxial compression results (not shown). Because in this case $E_{Sp} > E_{Br}$, no shifting was needed to adjust the moduli; they were simply mechanically shifted to pass through the origin.

It has long been appreciated that the Meyer hardness,

$$\frac{P}{\pi a^2} \approx 3\sigma_y \quad ,$$

where σ_y is the yield point.[2] It was thus gratifying to obtain the excellent agreement between uniaxial compression results and the indentation results [Fig. 7(b)]. Along the same lines, the indentation strain is related to the uniaxial strain, ϵ, by[2]

$$\frac{a}{R} \approx 5\epsilon \quad .$$

In Fig. 7(b), a factor of 10 was used instead of 5. The fit is good, in part because the moduli we determine from indentation in the case of Fe are significantly lower than the moduli measured under uniaxial loadings (Table I). The exact relationship between a/R and ϵ has not been studied in detail to date but is important that it be better understood. This is a fruitful area of research that we are embarking on.

The agreement between the Vickers microhardness values measured here and those shown in Fig. 7(b) must be considered excellent. The scatter is believed to be real and due to the polycrystalline nature of the sample. More careful work, especially on Fe single crystals, is indicated, however, to better understand the subtleties of the elastic-to-plastic transition and the effect of grain boundaries on the local deformation. Note that in this case our Berkovich hardness values are in excellent agreement with our Vickers microhardness results.

F. Aluminum

For reasons that are not clear, the moduli values for Al obtained from Fig. 2(a), are ≈30% lower than those reported for pure Al reported in the literature and ≈20% lower than E_{Br} (Table I). They are also lower than the value of 70 GPa reported by Herbert et al.[7] essentially using the same technique applied here. It is this large discrepancy that led us to introduce the δ-correction and explains why it is the greatest for that solid.

The hardness values measured herein are also roughly ⅓ of the values reported by Field and Swain[5] for pure Al. The reason for the discrepancy is unclear, but Field and Swain did not work with the CSM attachment. Also for reasons that are not clear, the indentation stress–strain curves derived by Herbert et al.[7] from spherical nanoindentation experiments on 6066-T1 Al—essentially using the same technique described here—obtained quite different results. In the same paper, the hardness values did not asymptote or reach a steady state, but continually increased with strain. Two possibilities for the discrepancy could be that Herbert et al. used an Al-alloy rather than pure Al and/or the fact that they used much larger spherical indenters. These discrepancies notwithstanding, there is little doubt that our quasi–steady-state hardness values are in good agreement with the Vickers microhardness values measured on the same Al [Fig. 3(a) and Table I], which is comforting.

VI. SUMMARY AND CONCLUSIONS

When load-penetration nanoindentation results, obtained with spherical indenters, are properly converted to indentation stress–strain curves, the latter can provide invaluable information about one of the most important

transitions in materials: the elastic-to-plastic transition; information that, as has long been appreciated, is lost when sharp indenters are used.[2] Indentation stress–strain curves can also shed light on work hardening, micro-yielding, or simply whether what is occurring under an indenter is dislocation-based or not.

In this article we combine the CSM measurements, with Hertzian theory, the Oliver and Pharr method, and Berkovich indentations to convert spherical nanoindentation load–displacement curves to indentation stress–strain curves. The results are judged by how closely they match the Vickers microhardness measurements on the same solids, the latter an easy, straightforward, but crucial criteria that, as far as we are aware, has never been previously used in conjunction with nanoindentation results. This comment notwithstanding, there is still much that must be learned. For example, in all cases examined here, the work hardening after the yield or pop-ins is not negligible. Whether this is an artifact of our method or a real effect is unclear at this time. Also why the "yield point" in Fig. 4(c) is higher than the one measured by Vickers indentations is not clear.

Lastly we hope that this work will stimulate others to continue refining this potentially very fruitful and versatile method to obtain indentation stress–strain curves.

ACKNOWLEDGMENTS

REFERENCES

1. W.C. Oliver and G.M. Pharr: Measurement of hardness and elastic modulus by instrumented indentation: Advances in understanding and refinements to methodology. *J. Mater. Res.* **19,** 3 (2004).
2. D. Tabor: *Hardness of Metals* (Clarendon Press, Oxford, 1951).
3. X. Li and B. Bhusan: A review of nanoindentation continuous stiffness measurement technique and its applications. *Mater. Charact.* **48,** 11 (2002).
4. J.S. Field and M.V. Swain: The indentation characterisation of the mechanical properties of various carbon materials: Glassy carbon, coke and pyrolytic graphite. *Carbon* **34,** 1357 (1996).
5. J.S. Field and M.V. Swain: Determining the mechanical properties of small volumes of material from submicrometer spherical indentations. *J. Mater. Res.* **10,** 101 (1995).
6. J.E. Bradby, J.S. Williams, and M.V. Swain: Pop-in events induced by spherical indentation in compound semiconductors. *J. Mater. Res.* **19,** 380 (2004).
7. E.G. Herbert, G.M. Pharr, W.C. Oliver, B.N. Lucas, and J.L. Hay: On the measurement of stress-strain curves by spherical indentation. *Thin Solid Films* **398–399,** 331 (2001).
8. N. Iwashita, M.V. Swain, J.S. Field, N. Ohta, and S. Bitoh: Elasto-plastic deformation of glass-like carbons heat-treated at different temperatures. *Carbon* **39,** 1525 (2001).
9. N. Iwashita, J.S. Field, and M.V. Swain: Indentation hysteresis of glassy carbon materials. *Philos. Mag. A* **82,** 1873 (2002).
10. J.S. Field and M.V. Swain: A simple predictive model for spherical indentation. *J. Mater. Res.* **8,** 297 (1993).
11. J.E. Bradby, S.O. Kucheyev, J.S. Williams, C. Jagadish, M.V. Swain, P. Munroe, and M.R. Phillips: Contact-induced defect propagation in ZnO. *Appl. Phys. Lett.* **80,** 4537 (2002).
12. S.O. Kucheyev, J.E. Bradby, J.S. Williams, C. Jagadish, and M.V. Swain: Mechanical deformation of single-crystal ZnO. *Appl. Phys. Lett.* **80,** 956 (2002).
13. A. Murugaiah, M.W. Barsoum, S.R. Kalidindi, and T. Zhen: Spherical Nanoindentations in Ti_3SiC_2. *J. Mater. Res.* **19,** 1139 (2004).
14. M.W. Barsoum, A. Murugaiah, S.R. Kalidindi, and T. Zhen: Kinking nonlinear elastic solids, nanoindentations and geology. *Phys. Rev. Lett.* **92,** 255508-1 (2004).
15. M.W. Barsoum, A. Murugaiah, S.R. Kalidindi, and Y. Gogotsi: Kink bands, nonlinear elasticity and nanoindentations in graphite. *Carbon* **42,** 1435 (2004).
16. I.N. Sneddon: The relaxation between load and penetration in the axisymmetric boussinesq problem for a punch of arbitrary profile. *Int. J. Eng. Sci.* **3,** 47 (1965).
17. B.N. Lucas and W.C. Oliver: Indentation power-law creep of high-purity indium. *Metall. Mater. Trans. A* **30,** 601 (1999).
18. S. Basu, M.W. Barsoum, and S.R. Kalidindi: Sapphire: A kinking nonlinear elastic solid. *J. Appl. Phys.* **99,** 063501 (2006).
19. U. Ozgur, Y.I. Alivov, C. Liu, A. Teke, M.A. Reshchikov, S. Dogan, V. Aurutin, S.J. Cho, and H. Morkoc: A comprehensive review of ZnO materials and devices. *J. Appl. Phys.* **98,** 041301 (2005).
20. J.B.J. Wachtman, W.E. Tefft, D.C.J. Lam, and R.P. Stenchfield: Elastic constants of synthetic single crystal corundum at room temperature. *J. Res. Natl. Bur. Stand.* **64A,** 213 (1960).